micro

MDPI

Article

Eri Silk Fibroin-Mediated Biosynthesis of Silver Nanoparticles with In Vitro Antibacterial Activity Against *Vibrio parahaemolyticus*

Pisutsaran Chitichotpanya [1,*], Nattaya Vuthiganond [1], Penwisa Pisitsak [1], Manthana Jariyaboon [2,3] and Chayanisa Chitichotpanya [2,3]

[1] Department of Materials and Textile Technology, Faculty of Science and Technology, Thammasat University, Pathum Thani 12120, Thailand; pnattaya@tu.ac.th (N.V.); penwisa@tu.ac.th (P.P.)
[2] Department of Chemistry, Faculty of Science, Mahidol University, Bangkok 10400, Thailand; manthana.jar@mahidol.ac.th (M.J.); chayanisa.chi@mahidol.ac.th (C.C.)
[3] Center for Surface and Engineering, Faculty of Science, Mahidol University, Nakhon Pathom 73170, Thailand
* Correspondence: pisut_c@tu.ac.th

Abstract

The emergence of antibiotic-resistant *Vibrio parahaemolyticus* poses a challenge to sustainable shrimp aquaculture and highlights the need for effective antibacterial alternatives. In this study, silver nanoparticles were biosynthesized using Eri silk fibroin (ESF) as both a reducing and stabilizing biopolymer. Eri silkworms can be reared on cassava leaves, an abundant agricultural by-product in Thailand, thereby supporting waste valorization and the circular bioeconomy. Optimal synthesis was achieved at an $AgNO_3$-to-ESF weight ratio of 1:4, 60 °C, and 4 h, yielding 82.8% ESF-AgNPs with a particle size of 10.8 ± 2.3 nm and a polydispersity index of 0.19 ± 0.01. TEM, XRD, and XPS confirmed the formation of well-dispersed metallic Ag^0. The particles remained colloidally stable for at least four weeks. ESF-AgNPs exhibited minimum inhibitory and bactericidal concentrations of 12.5 and 25 μg/mL, respectively; inhibited biofilm formation by 52.45–99.98%; and increased intracellular reactive oxygen species generation. After 72 h, silver release reached 5.70% in deionized water and 9.30% in TSB containing 3% NaCl. *Artemia franciscana* survival remained 96.2% after 24 h at the MBC. These findings support ESF as a sustainable platform for producing antibacterial and antibiofilm AgNPs with a preliminary safety margin, although further in vivo efficacy and chronic-toxicity studies are required before practical application.

Keywords: Eri silk fibroin; silver nanoparticles; green synthesis; *Vibrio parahaemolyticus*; antibacterial activity; antibiofilm activity; shrimp

Check for updates

Academic Editor: Xiaopeng Huang

Received: 14 July 2026
Revised: 31 July 2026
Accepted: 5 August 2026
Published: 11 August 2026

Copyright: © 2026 by the authors. Licensee MDPI, Basel, Switzerland. This article is an open access article distributed under the terms and conditions of the Creative Commons Attribution (CC BY) license.

1. Introduction

Shrimp is a nutritionally valuable and economically important food source. The shrimp aquaculture industry has expanded rapidly worldwide, particularly in Thailand, and is recognized as one of the most valuable sectors of global aquaculture [1,2]. However, the intensification of shrimp farming, together with high stocking densities and suboptimal management practices, has increased the incidence and severity of infectious diseases. Among these diseases, acute hepatopancreatic necrosis disease (AHPND), caused by pathogenic *Vibrio parahaemolyticus*, is one of the most devastating diseases affecting cultured shrimp [3]. *V. parahaemolyticus* is a halophilic Gram-negative bacterium belonging

to the family Vibrionaceae and is commonly found in marine and aquaculture environments [4]. Pathogenic strains carrying the *pirA* and *pirB* toxin genes are responsible for AHPND, which causes severe hepatopancreatic damage, high mortality, and substantial economic losses in shrimp farming. Since its first emergence, AHPND has spread rapidly across many Asian countries and remains a major constraint to the sustainable development of the shrimp aquaculture industry [5,6]. Beyond aquaculture, *V. parahaemolyticus* is also an important foodborne pathogen that can cause acute gastroenteritis in humans and is recognized as one of the major enteric bacterial pathogens worldwide [7]. Moreover, resistance to multiple antibiotics, including ampicillin, rifampicin, and streptomycin, has been widely reported in *V. parahaemolyticus* [8–10]. The overuse and misuse of antibiotics in aquaculture have accelerated the emergence of resistant bacterial strains, posing serious risks to aquatic animals, consumers, and public health [11]. Therefore, the rapid rise of antibiotic-resistant bacteria highlights the urgent need for alternative antibacterial strategies that can overcome the limitations of conventional antibiotics.

Silver nanoparticles (AgNPs), a representative class of metal-based nanomaterials, have attracted considerable attention because of their potent and broad-spectrum antimicrobial properties [12]. Their antibacterial activity is mainly associated with their large surface area, redox reactivity, ability to generate oxidative stress, and capacity to disrupt microbial cell membranes [13]. AgNPs have demonstrated antimicrobial efficacy against a wide range of microorganisms, including viruses, bacteria, and fungi. In shrimp aquaculture, AgNPs have also shown effectiveness against *Vibrio* species in several shrimp species, including *Fenneropenaeus indicus*, *Penaeus monodon*, and *Litopenaeus vannamei* [14]. Nevertheless, conventional chemical synthesis methods for AgNPs often involve hazardous reagents, which may generate harmful byproducts and limit their practical application in environmentally sensitive systems such as aquaculture [15]. Therefore, the development of green, biocompatible, and sustainable methods for AgNP synthesis has become increasingly important.

In Asia and the Pacific region, the Eri silkworm (*Samia ricini*) can be cultivated sustainably because of its high productivity and good adaptation to tropical climates [16]. Unlike the mulberry silkworm (*Bombyx mori*), which relies primarily on mulberry leaves, Eri silkworms can be reared on cassava leaves, an abundant agricultural residue generated from cassava cultivation. The use of cassava leaves as a low-cost feed resource can reduce production costs, promote agricultural waste valorization, and support the circular bioeconomy. This advantage is particularly relevant to Thailand, one of the world's major cassava-producing countries and a leading exporter of tapioca starch. Silk fibers are composed primarily of two proteins: fibroin and sericin [17]. Fibroin is the main structural protein and consists of repetitive amino acid sequences flanked by N- and C-terminal domains, whereas sericin acts as an adhesive protein that surrounds and binds the fibroin fibers. Among these proteins, silk fibroin (SF) has attracted considerable interest as a sustainable biopolymer for nanoparticle fabrication because of its excellent mechanical properties, tunable biodegradability, high thermal stability, low immunogenicity, and biocompatibility. SF also contains hydroxyl, carboxyl, and amino functional groups that enable it to function as both a reducing template and a stabilizing matrix during nanoparticle synthesis [18]. Its β-sheet-rich secondary structure contributes to its mechanical strength and structural integrity and, based on previous studies, may provide a stable framework that limits nanoparticle aggregation.

Previous studies have demonstrated the successful biosynthesis of AgNPs using SF derived mainly from B. mori [19,20]. SF contains 18 amino acids and abundant polar functional groups that can provide reactive sites for nanoparticle nucleation, surface coordination, and stabilization. In particular, tyrosine residues have been identified as important

reducing sites that facilitate the conversion of Ag^+ ions into metallic Ag^0 atoms, followed by nanoparticle nucleation and growth, as illustrated in Figure 1. The fibroin matrix may subsequently stabilize the formed nanoparticles, limit their aggregation and oxidation, and influence Ag^+ ion release, thereby improving nanoparticle stability and functionality [21]. Consequently, SF has been widely investigated as a protein-based biotemplate for controlling the size, morphology, and colloidal stability of AgNPs. Despite these advances, most previous studies have focused on fibroin derived from B. mori, whereas the use of Eri silk fibroin (ESF) remains comparatively limited. ESF has been reported to contain a higher tyrosine content than B. mori fibroin, with values of approximately 5.63% and 4.59%, respectively [19]. Because tyrosine residues can participate in Ag^+ reduction, this compositional difference provides an additional functional rationale for selecting ESF as a biotemplate for AgNP synthesis. Moreover, its relatively well-defined protein composition and abundant polar functional groups allow ESF to function as both a reducing and stabilizing matrix. Compared with plant extracts [22], which may exhibit considerable variation in phytochemical composition, ESF may provide a more consistent protein-based platform. In addition, the use of Eri silk obtained from silkworms reared on locally available cassava leaves supports the sustainable and value-added utilization of regional biological resources. Although ESF-mediated AgNP biosynthesis has previously been reported [23], earlier work primarily focused on nanoparticle synthesis, broad-spectrum antibacterial activity, and photocatalytic dye degradation. Our study extends this research through the systematic optimization of ESF-mediated AgNP biosynthesis and the first targeted evaluation of the resulting nanoparticles against *V. parahaemolyticus*. This evaluation included MIC and MBC determination, antibiofilm activity, reactive oxygen species (ROS) generation, silver-release behavior, and preliminary aquatic toxicity toward *Artemia franciscana*, thereby providing a more comprehensive assessment of the physicochemical properties, antibacterial activity, and preliminary biosafety of ESF-AgNPs.

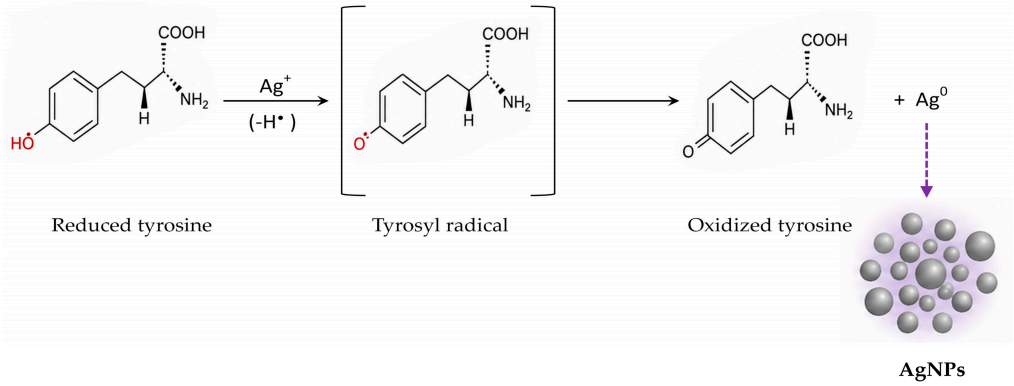


Figure 1. Proposed schematic mechanism of tyrosine-reducing silver ions.

This study focused on the biosynthesis and physicochemical characterization of ESF-AgNPs, together with a preliminary in vitro evaluation of their antibacterial and antibiofilm activities against *V. parahaemolyticus*. Silver-release analysis and an acute toxicity assay using *A. franciscana* were also conducted to provide preliminary information on silver behavior and short-term biosafety. However, these assessments were not intended to constitute a comprehensive ecological risk evaluation or to establish the environmental safety of ESF-AgNPs for practical aquaculture use. Further studies addressing chronic toxicity, bioaccumulation, environmental fate, trophic transfer, shrimp safety, and potential effects on other non-target aquatic organisms are therefore required before practical application can be considered.

2. Materials and Methods

2.1. Materials

The Eri silk cocoons were procured from the Nong Ya Plong Community, Mancha Khiri, Khon Kaen Province, Thailand. Silver nitrate ($AgNO_3$, 99.8% purity), sodium carbonate (Na_2CO_3), and calcium nitrate ($Ca(NO_3)_2$) were purchased from Carlo Erba Reagents (Bangkok, Thailand). All other chemicals applied throughout this work were analytical quality and obtained from Sigma-Aldrich (Bangkok, Thailand).

2.2. Extraction of Eri Silk Fibroin (ESF)

Eri silk cocoons were first cut into small pieces and subjected to a degumming process to remove the sericin coating from the SF fibers. Degumming was performed by boiling the cocoon pieces in 0.02 M Na_2CO_3 solution for 1 h. The resulting degummed SF was thoroughly rinsed twice with distilled water to remove residual sericin and Na_2CO_3, followed by air drying at room temperature. The extraction of ESF was then carried out using a dissolution method adapted from a previously reported ESF extraction procedure [24]. Briefly, the dried degummed Eri silk was dissolved in a ternary solvent system composed of $Ca(NO_3)_2$, ethanol, and deionized water at a ratio of 1:4:1.5. The dissolution process was conducted at 100 °C for 8 h using an infrared dyeing machine (Starlet DL-6000, Daelim Starlet Co., Ltd., Gyeonggi-do, Siheung-si, South Korea). After dissolution, the obtained ESF solution was transferred into a dialysis membrane and dialyzed against DI water for 3 days to remove residual salts and solvent components. The dialysis water was replaced every 24 h. The dialyzed ESF solution was subsequently centrifuged at 5000 rpm for 10 min to eliminate undissolved silk residues. Finally, the purified ESF solution was lyophilized into powder form using an Alpha 3-4 LSCbasic freeze-dryer (Martin Christ Gefriertrocknungsanlagen GmbH, Osterode am Harz, Germany).

2.3. Biosynthesis of ESF-AgNPs

ESF-AgNPs were prepared using ESF extract, which functioned as both the reducing and stabilizing agent. Effects of key reaction parameters, including the $AgNO_3$-to-ESF weight ratio, reaction temperature, and reaction time, were systematically investigated. $AgNO_3$ and ESF extract powder were mixed at varied weight ratios (1:2, 1:4, and 1:8) in 200 mL of deionized (DI) water and stirred vigorously. A noticeable color change from light green to yellowish-brown signified the successful formation of ESF-AgNPs. The synthesis procedure was further conducted at different temperatures (30, 45, and 60 °C) and reaction times (2, 4, and 6 h) to evaluate their influence on nanoparticle formation. The obtained ESF-AgNPs were characterized using a UV–visible spectrophotometer (Shimadzu UV-1800, Shimadzu Corporation, Kyoto, Japan) over a wavelength range of 325–700 nm to determine the optimal synthesis conditions. In addition, the hydrodynamic particle size and zeta potential of the biosynthesized AgNPs were measured using a Zetasizer Nano ZS (ZEN 3600, Malvern Instruments Ltd., Malvern, Worcestershire, UK) to evaluate their size distribution and colloidal stability. Before analysis, the ESF-AgNP suspension was diluted 25-fold (1:25, v/v) with DI water. Zeta-potential measurements were conducted at neutral pH. All measurements were performed in triplicate at 25 °C.

Subsequently, the AgNP yield was calculated as the ratio of the mass of elemental silver recovered in the nanoparticle fraction to the initial mass of silver added as $AgNO_3$ during the synthesis reaction. The AgNP yield was determined using a method adapted from Agnihotri et al. [25]. Briefly, the AgNP suspensions were centrifuged at 14,000 rpm for 20 min to separate the nanoparticles from soluble and unreacted reaction components. The collected AgNP pellets were completely digested in HNO_3, and the total mass of elemental

silver in the nanoparticle fraction was quantified using inductively coupled plasma mass spectrometry (ICP-MS; NexION 2000, PerkinElmer Inc., Shelton, CT, USA).

2.4. Characterization of AgNPs

The morphological characteristics of the biosynthesized AgNPs were examined using transmission electron microscopy (TEM; JEM-2100, JEOL Ltd., Akishima, Tokyo, Japan) operated at an accelerating voltage of 200 kV. A drop of the AgNP suspension was deposited onto carbon-coated copper grids and allowed to dry under ambient conditions prior to analysis. Particle size distribution was determined by measuring approximately 230 NPs using ImageJ software (version 1.54p, National Institutes of Health, Bethesda, MD, USA). The crystalline structure of the NPs was investigated by X-ray diffraction (XRD; D8 DISCOVER, Bruker AXS GmbH, Karlsruhe, Germany) over a 2θ range of 25–80°, employing Cu Kα radiation at 40 kV and 40 mA, with a scanning rate of 6°/min. Average crystallite size was estimated via the Scherrer equation [26]:

$$D = \frac{k\lambda}{\beta\cos\theta} \quad (1)$$

where D is the crystallite size (nm), k is the shape factor (0.9), λ is the X-ray wavelength (nm), β is the full width at half maximum (FWHM), and θ is the Bragg angle.

The surface elemental composition and chemical states were further examined by X-ray photoelectron spectroscopy (XPS; AXIS Ultra DLD, Kratos Analytical Ltd., Manchester, UK), and the obtained spectra were processed using Vision II software (version 2.2.6, Kratos Analytical Ltd., Manchester, UK).

2.5. Assessment of Antibacterial Activity

2.5.1. Determination of the Minimum Inhibitory Concentration

The minimum inhibitory concentration (MIC) was defined as the lowest concentration of ESF-AgNPs that completely inhibited visible bacterial growth. The MIC against *V. parahaemolyticus* was determined using the broth microdilution method based on the CLSI guidelines (2014) [27], with minor modifications. An AHPND-associated isolate of *V. parahaemolyticus* was obtained from the Aquaculture Business Research Center (ABRC), Faculty of Fisheries, Kasetsart University, Thailand. The isolate was identified as *V. parahaemolyticus* by the providing laboratory. However, the strain-level molecular identification and detection of the *pirA* and *pirB* toxin genes were not independently performed in the present study. Before the assay, the isolate was subcultured twice on Tryptic Soy Agar (TSA) supplemented with 1.5% (*w*/*v*) NaCl and incubated at 37 °C for 24 h. Bacterial cells were collected by centrifugation at 1000 rpm for 15 min, resuspended in sterile 1.5% (*w*/*v*) NaCl solution, and adjusted to an optical density of 0.1 at 625 nm, corresponding to approximately 10^8 CFU/mL CFU/mL. Two-fold serial dilutions of ESF-AgNPs were prepared in Tryptic Soy Broth (TSB) supplemented with 3% (*w*/*v*) NaCl in sterile 96-well microplates. After inoculation, the final ESF-AgNP concentrations ranged from 0.78 to 400 µg/mL, and the final bacterial density was adjusted to 10^6 CFU/mL. The plates were incubated aerobically at 37 °C for 24 h. The MIC was recorded as the lowest ESF-AgNP concentration showing no visible turbidity. Inoculated medium without ESF-AgNPs served as the growth control, whereas chloramphenicol at 30 µg/mL was used as the reference antibiotic control. The assay was performed using five replicate wells.

2.5.2. Determination of the Minimum Bactericidal Concentration

The minimum bactericidal concentration (MBC) was defined as the lowest ESF-AgNP concentration producing a ≥99.9% reduction in the viable bacterial population relative to

the initial inoculum. Following the MIC assay, aliquots were collected from wells containing ESF-AgNPs at the MIC and higher concentrations. The samples were serially diluted in sterile 1.5% (*w*/*v*) NaCl, and 100 µL of each appropriate dilution was spread onto TSA supplemented with 1.5% (*w*/*v*) NaCl. After aerobic incubation at 37 °C for 24 h, countable colonies were enumerated, and viable-cell populations were expressed as CFU/mL. Two relevant equations are shown below:

$$\text{Log reduction} = \log_{10} N_0 - \log_{10} N_t$$

$$\%\ \text{Reduction} = \left(\frac{N_0 - N_t}{N_0}\right) \times 100$$

where (N_0) is the initial viable count and (N_t) is the viable count after 24 h of treatment. The MBC was identified as the lowest concentration producing a reduction of at least 3$\log_{10}$ CFU/mL, equivalent to ≥99.9% bacterial killing. When no colonies were detected, viable counts were reported as below the detection limit rather than as zero CFU/mL. The MBC assay was performed in three independent experiments.

2.6. Antibiofilm Activity

The antibiofilm activity was assessed using a crystal violet microtiter plate assay adapted from Yuan et al. [28]. Briefly, 200 µL of *V. parahaemolyticus* suspension containing ESF-AgNPs at final concentrations equivalent to 0.25 MIC, 0.5 MIC, 1 MIC, and 2 MIC was transferred into individual wells of a sterile 96-well polystyrene microplate. The plate was incubated at 37 °C for 24 h to allow biofilm formation. After incubation, the culture medium was carefully removed, and each well was rinsed three times with phosphate-buffered saline (PBS) to eliminate non-adherent and planktonic cells. The remaining attached biofilm was fixed with 200 µL of methanol for 15 min, after which the methanol was discarded. The fixed biofilms were stained with 0.3% crystal violet for 15 min and subsequently rinsed with sterile distilled water until the unbound dye was completely removed. After air-drying, the retained crystal violet was solubilized using 33% acetic acid. Biofilm biomass was quantified by measuring the absorbance at 590 nm using a microplate reader (Cytation 3, BioTek Instruments, Inc., Winooski, VT, USA). Wells containing the bacterial suspension without ESF-AgNPs served as the untreated controls. The percentage inhibition of biofilm formation was calculated using the following equation:

$$\%\ \text{Biofilm inhibition} = 1 - \frac{A_i}{A_0} \times 100$$

where A_i and A_0 are the absorbance values with and without ESF-AgNPs, respectively.

2.7. Reactive Oxygen Species (ROS) Assay

Intracellular ROS generation was evaluated using the 2′,7′-dichlorofluorescein diacetate (DCFH-DA) assay [29]. *V. parahaemolyticus* cells were washed twice and resuspended in salt-adjusted PBS at approximately 1 × 10^6 CFU/mL. The bacterial suspension was incubated with 10 µM DCFH-DA at 37 °C for 2 h and subsequently washed twice to remove excess dye. The stained bacterial cells were then treated with ESF-AgNPs at 0, 0.5 MIC, 1 MIC, and 1 MBC, corresponding to 0, 6.25, 12.5, and 25 µg/mL, respectively. Fluorescence intensity was measured using a Synergy HTX multimode microplate reader (BioTek Instruments, Winooski, VT, USA) at excitation and emission wavelengths of 485 and 528 nm, respectively. All experiments were performed in triplicate.

2.8. Assessment of Silver Release from ESF-AgNPs

Silver release from ESF-AgNPs was quantified using centrifugal ultrafiltration followed by ICP-MS analysis, according to a method adapted from [30]. The ESF-AgNP suspension was centrifuged at 10,000 for 30 min and washed three times with DI water. An aliquot of the purified suspension was completely digested with HNO_3 and analyzed by ICP-MS to determine the initial total elemental silver concentration. The purified ESF-AgNPs at 25 µg/mL, corresponding to the MBCs, were dispersed in DI water and sterile TSB supplemented with 3% NaCl. Triplicate sacrificial tubes were incubated at 37 °C in the dark with shaking at 100 rpm and collected at 0, 1, 2, 4, 8, 12, 24, 48, and 72 h. Samples were filtered and the filtrates were acidified and analyzed by ICP-MS. Silver release was calculated as

$$\% \text{ Silver release} = \frac{M_{released,\,t}}{M_{total,\,0}} \times 100$$

where $M_{released,\,t}$ is the silver mass in the filtrate and $M_{total,\,0}$ is the initial total silver mass. The results were expressed as mean ± SD of three replicates.

2.9. Toxicity Assay

The acute toxicity of ESF-AgNPs toward *Artemia franciscana* nauplii was evaluated using a method adapted from ISO/TS 20787 [31,32]. Approximately 25 nauplii were transferred into each well of a sterile six-well culture plate. Each well contained 4.5 mL of sterile artificial seawater, 1.0 mL of nauplius suspension, and 0.5 mL of ESF-AgNP treatment suspension, resulting in a final volume of 6.0 mL. ESF-AgNPs were tested at final concentrations of 6.25, 12.5, 25, 50, and 100 µg/mL, corresponding to 0.5 MIC, 1 MIC, 1 MBC, 2 MBC, and 4 MBC, respectively. All treatments were performed in triplicate. Wells containing nauplii in artificial seawater without ESF-AgNPs served as the negative control. An ESF-only treatment was included to evaluate the potential toxicity of the fibroin matrix, while potassium dichromate was used as the positive control. During the 24 h exposure period, the nauplii were maintained without feeding or aeration and examined every 6 h using a stereomicroscope. Nauplii showing active swimming or appendage movement were considered alive, whereas those exhibiting no movement after gentle agitation were recorded as dead. The survival percentage was calculated using the following equation:

$$\% \text{ Survival} = \frac{N_t}{N_0} \times 100$$

where N_t and N_0 is the number of live nauplii at time t and at the beginning of the experiment.

2.10. Statistical Examination

Statistical analyses were performed using IBM SPSS Statistics version 20 (IBM Corp., Armonk, NY, USA). Data are presented as the mean ± standard deviation (SD) of three in-dependent replicates (n = 3). Differences among groups were analyzed using one-way analysis of variance (ANOVA). Differences were considered statistically significant at $p < 0.05$.

3. Results and Discussion

3.1. Effect of Synthesis Conditions on the Optical and Physicochemical Properties of ESF-AgNPs

The effects of reaction temperature, reaction time, and the $AgNO_3$-to-ESF weight ratio on ESF-AgNP formation were evaluated using UV–visible spectroscopy together with yield, particle size, zeta potential, and the polydispersity index (PDI). As shown in Figure 2, all samples exhibited characteristic localized surface plasmon resonance (LSPR) bands at

approximately 404–415 nm, confirming AgNP formation [33]. The color change in the reaction mixtures to yellowish-brown or dark brown further indicated the reduction of Ag^+ ions to metallic Ag^0. Therefore, the spectroscopic results were consistent with the physicochemical properties presented in Table 1.

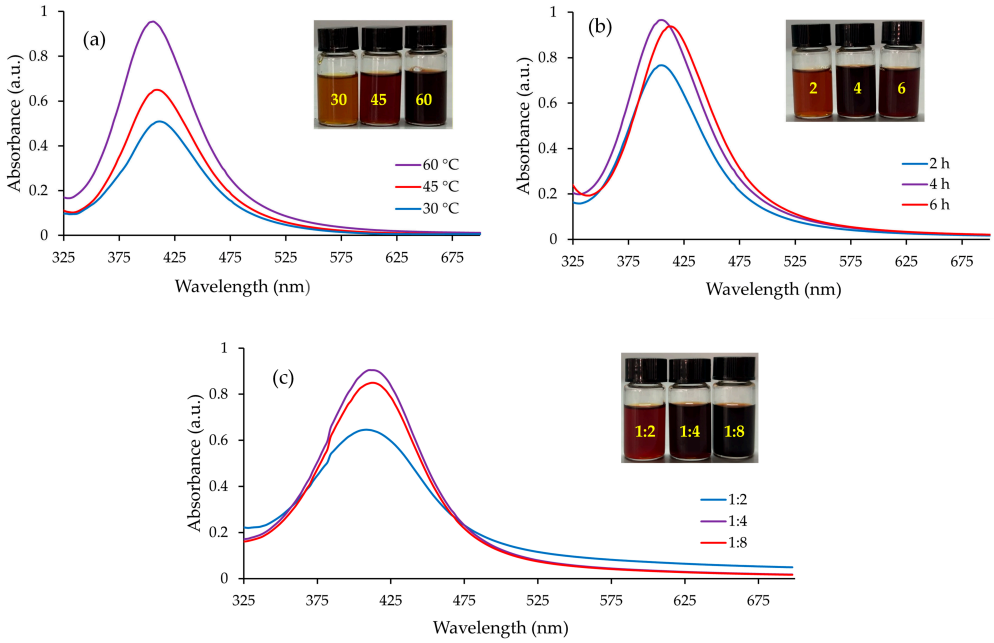


Figure 2. UV–vis absorption spectra of AgNPs synthesized using ESF extract under varied synthesis parameters: (**a**) temperature, (**b**) time, and (**c**) the $AgNO_3$-to-ESF extract weight ratio.

Table 1. Synthesis conditions and properties of ESF-AgNPs.

Sample	$AgNO_3$:ESF Weight Ratio	Temperature (°C)	Time (h)	Yield (%)	Particle Size (nm)	Zeta Potential	PDI
1	1:4	30	3	59.4	12.6 ± 4.1	−28.4 ± 2.6	0.39 ± 0.06
2	1:4	45	3	62.2	11.6 ± 2.9	−30.4 ± 2.7	0.31 ± 0.05
3	1:4	60	3	66.9	10.9 ± 2.7	−34.5 ± 2.0	0.28 ± 0.03
4	1:4	60	2	63.9	10.2 ± 3.8	−32.1 ± 2.3	0.29 ± 0.04
5	1:4	60	4	82.8	10.8 ± 2.3	−38.1 ± 2.4	0.19 ± 0.01
6	1:4	60	6	80.1	11.4 ± 2.5	−37.0 ± 2.4	0.21 ± 0.02
7	1:2	60	4	70.6	12.9 ± 3.1	−29.2 ± 2.3	0.28 ± 0.04
8	1:4	60	4	82.0	11.0 ± 2.1	−38.9 ± 2.6	0.18 ± 0.01
9	1:8	60	4	73.3	14.7 ± 4.5	−30.2 ± 1.9	0.36 ± 0.05

At a fixed $AgNO_3$-to-ESF weight ratio of 1:4 and a reaction time of 3 h, increasing the temperature from 30 to 60 °C progressively shifted the LSPR peak from 415 to 408 nm. This blue shift was consistent with the decrease in particle size from 12.6 ± 4.1 nm at 30 °C to 10.9 ± 2.7 nm at 60 °C. The nanoparticle yields simultaneously increased from 59.4% to 66.9%. These findings suggest that higher temperatures enhanced the interaction between Ag^+ ions and the reducing functional groups of ESF, thereby accelerating nucleation. At lower temperatures, slower reduction may generate fewer nuclei, allowing greater particle growth, whereas higher temperatures promote rapid nucleation and consequently produce smaller nanoparticles [34]. Increasing the temperature also improved particle uniformity and colloidal stability. The PDI decreased from 0.39 ± 0.06 at 30 °C to 0.28 ± 0.03 at 60 °C, indicating a narrower particle-size distribution. Meanwhile, the zeta potential became more negative, changing from −28.4 ± 2.6 to −34.5 ± 2.0 mV. The greater negative surface charge may result from more effective adsorption or exposure of negatively charged

ESF functional groups on the AgNP surfaces. Our findings are in agreement with those reported by Gwada et al. [35]. Therefore, synthesis at 60 °C favored the formation of smaller, more uniform, and more stable nanoparticles. The effect of reaction time was examined at 60 °C using an $AgNO_3$-to-ESF weight ratio of 1:4. LSPR peaks were detected at 406, 406, and 412 nm after 2, 4, and 6 h, respectively. Although the peak positions at 2 and 4 h were similar, the absorbance increased after 4 h, consistent with the increase in yield from 63.9% to 82.8%. The zeta potential also became more negative, changing from -32.1 ± 2.3 to -38.1 ± 2.4 mV, while the PDI decreased from 0.29 ± 0.04 to 0.19 ± 0.01. These results indicate that 4 h provided sufficient time for efficient Ag^+ reduction and effective stabilization of the newly formed nanoparticles by ESF. Further extension of the reaction time to 6 h caused the LSPR peak to shift from 406 to 412 nm and increased the particle size slightly from 10.8 ± 2.3 to 11.4 ± 2.5 nm. The gradual red shift suggests an increase in particle size, attributable to Ostwald ripening, wherein larger particles expand at the expense of smaller ones over time [36]. The yield decreased slightly to 80.1%, while the PDI increased to 0.21 ± 0.02. These changes suggest that nanoparticle formation was largely completed within 4 h and that prolonged heating promoted limited particle growth or aggregation. The $AgNO_3$-to-ESF weight ratio also influenced nanoparticle formation. At 60 °C for 4 h, samples prepared at ratios of 1:2, 1:4, and 1:8 exhibited LSPR peaks at 404, 407, and 406 nm, with absorbance values of approximately 0.65, 0.90, and 0.85 a.u., respectively. The 1:4 ratio produced the highest absorbance and yield of approximately 82%, compared with 70.6% at 1:2 and 73.3% at 1:8. At the 1:2 ratio, the lower ESF content may have provided insufficient reducing and capping functional groups, resulting in a larger particle size of 12.9 ± 3.1 nm, a less negative zeta potential of -29.2 ± 2.3 mV, and a PDI of 0.28 ± 0.04. Increasing the ESF proportion to 1:4 produced particles of approximately 11 nm, with a zeta potential of about −38 mV and a low PDI of 0.18–0.19, indicating a suitable balance between Ag^+ reduction and nanoparticle stabilization. In contrast, the 1:8 ratio produced larger and more polydisperse particles (14.7 ± 4.5 nm; PDI 0.36 ± 0.05), possibly because excess ESF increased medium viscosity, limited mass transfer, or promoted inter-molecular bridging. Based on the combined UV–visible and physicochemical results, the optimal synthesis conditions were an $AgNO_3$-to-ESF weight ratio of 1:4 at 60 °C for 4 h, providing high yield, small and uniformly distributed particles, and good colloidal stability.

3.2. Characterization of ESF-AgNPs

The FTIR spectra of ESF and ESF-AgNPs provide evidence for the involvement of SF functional groups in the biosynthesis and stabilization of AgNPs. As shown in Figure 3, the broad absorption band centered at approximately 3279 cm^{-1} in the ESF spectrum is assigned to the amide A band, which primarily originates from N–H stretching vibrations with partial overlap from the O–H stretching vibrations of the phenolic hydroxyl groups of tyrosine residues in the ESF chain [23]. Following AgNP synthesis, this band shifted from 3279 to 3284 cm^{-1}, exhibiting a blue shift that indicates interactions between SF functional groups and the nanoparticle surface. The FTIR spectrum of ESF also displayed three characteristic amide bands at approximately 1227, 1513, and 1618 cm^{-1}, corresponding to amide III, amide II, and amide I, respectively [18]. These bands are characteristic of the β-sheet-rich secondary structure of ESF [37]. After AgNP formation, the corresponding bands shifted to approximately 1233, 1519, and 1625 cm^{-1}, respectively, indicating blue shifts relative to pristine ESF. In addition, the absorption peak at 1160 cm^{-1}, assigned to the C–O stretching vibration of the phenolic hydroxyl group of tyrosine residues, shifted to 1165 cm^{-1} after AgNP synthesis. The blue shifts observed for the amide A-, amide I-, amide II-, amide III-, and tyrosine-associated C–O stretching bands indicate that both the hydroxyl and amide functional groups of ESF participate in the formation of AgNPs. In particular, the

shift of the tyrosine-associated band suggests that the phenolic hydroxyl groups of tyrosine residues are involved in the reduction of Ag^+ ions and/or the stabilization of the resulting NPs. These findings indicate that ESF functions as both a reducing agent, facilitating the conversion of Ag^+ to Ag^0, and a stabilizing agent by coordinating its functional groups with the nanoparticle surface, thereby suppressing nanoparticle aggregation. Furthermore, the preservation of the characteristic β-sheet-associated amide bands after AgNP synthesis indicates that the β-sheet-rich secondary structure of silk fibroin remained intact throughout the biosynthesis process.

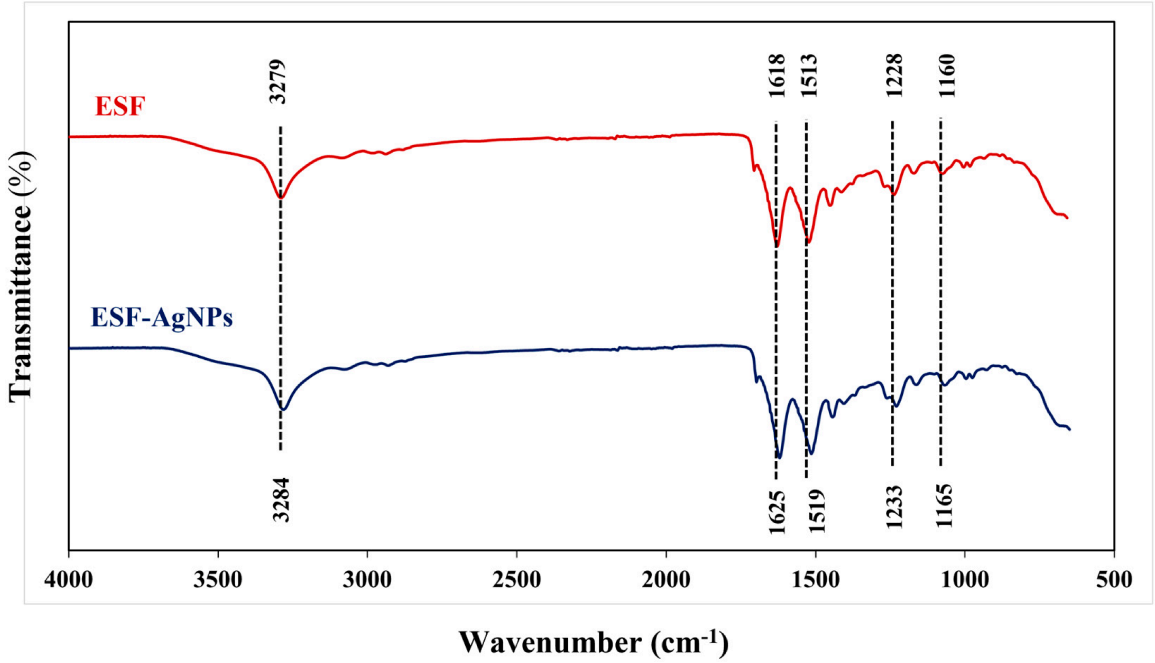


Figure 3. FTIR spectrum of ESF and biosynthesized ESF-AgNPs.

Figure 4 illustrates the XRD patterns of the biosynthesized ESF-AgNPs, which were analyzed to evaluate their crystallinity and crystallite size. The diffraction pattern exhibits characteristic peaks at approximately 38.97°, 46.45°, 64.25°, and 77.53° (2θ), correlated to the (111), (200), (220), and (311) planes of the crystalline structure, respectively. These reflections are indicative of the face-centered cubic (fcc) crystal structure of metallic Ag and are consistent with the standard JCPDS file No. 04-0783. The obtained results are in good agreement with those of a previously reported study [22]. In addition to the main diffraction peaks, minor peaks observed in the spectrum may be attributed to residual biomolecules from the ESF extract or the presence of amorphous phases. The average crystallite size of the AgNPs, calculated using the Debye–Scherrer equation (Equation (1)), was determined to be 13.9 nm.

The oxidation state of silver in the synthesized ESF-AgNPs was further examined using XPS. The high-resolution Ag 3d XPS spectrum is presented in Figure 5. Two prominent peaks were observed at binding energies of 368.5 eV and 374.5 eV, corresponding to Ag $3d_{5/2}$ and Ag $3d_{3/2}$, respectively, with a spin–orbit splitting of 6.0 eV. These values are characteristic of metallic silver (Ag^0), confirming the successful reduction of Ag^+ ions during the biosynthesis process [37]. For comparison, the standard binding energies of pure metallic silver are typically reported at approximately 368.1 eV and 374.1 eV [38]. The slight shift of the Ag 3d peaks toward lower binding energies in ESF-AgNPs may be attributed to electronic interactions between the nanoparticle surface and biomolecules present in the SF extract, leading to charge transfer effects. Similar shifts in binding

energy have been reported in previous studies on biosynthesized AgNPs, including those mediated by protein-based systems such as peptone (Pep) [39] and soy protein [40], thereby supporting the proposed interaction mechanism.

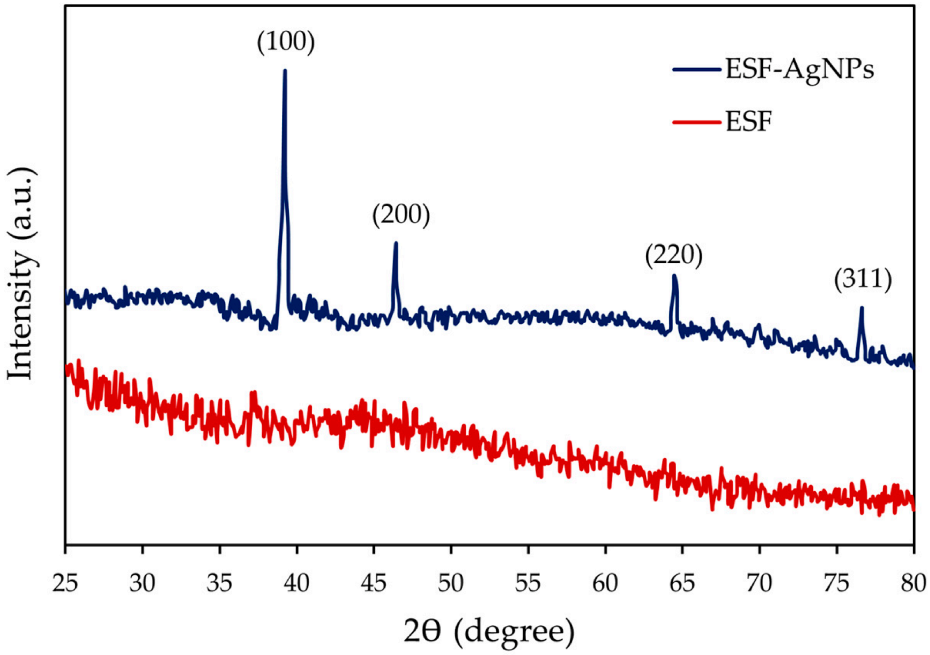


Figure 4. XRD patterns of biosynthesized ESF-AgNPs.

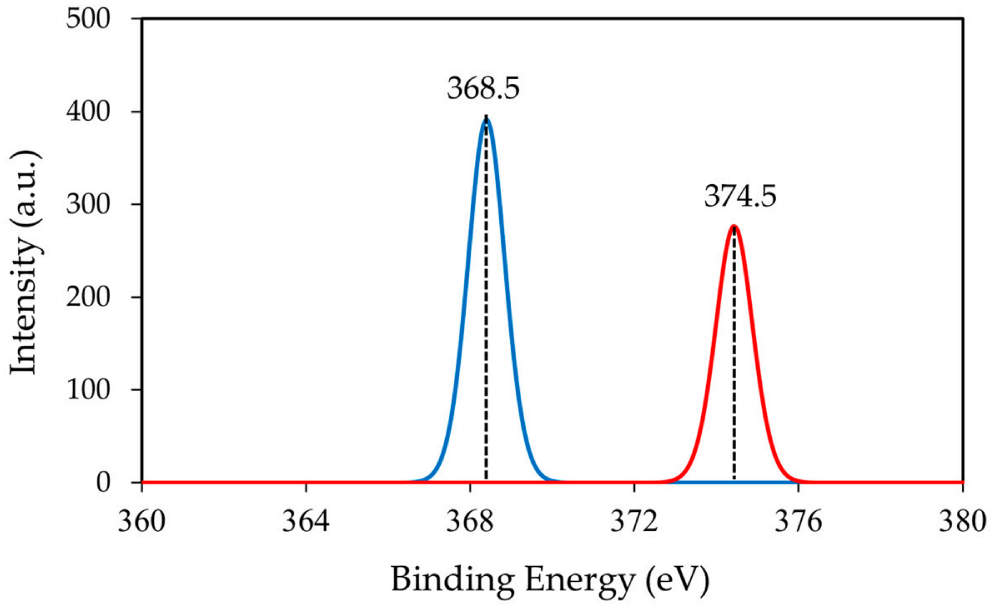


Figure 5. Deconvoluted Ag 3d XPS spectrum of ESF-AgNPs, showing Ag $3d_5/_2$ peak (blue) and Ag $3d_3/_2$ peak (red).

The morphology and particle size of the biosynthesized ESF-AgNPs, as revealed by TEM analysis, are shown in Figure 6. The nanoparticles were predominantly spherical and well dispersed, with a mean particle size of 10.3 ± 3.8 nm (Figure 6c). This value was consistent with the crystallite size estimated from XRD analysis, confirming the successful formation of AgNPs using ESF extract.

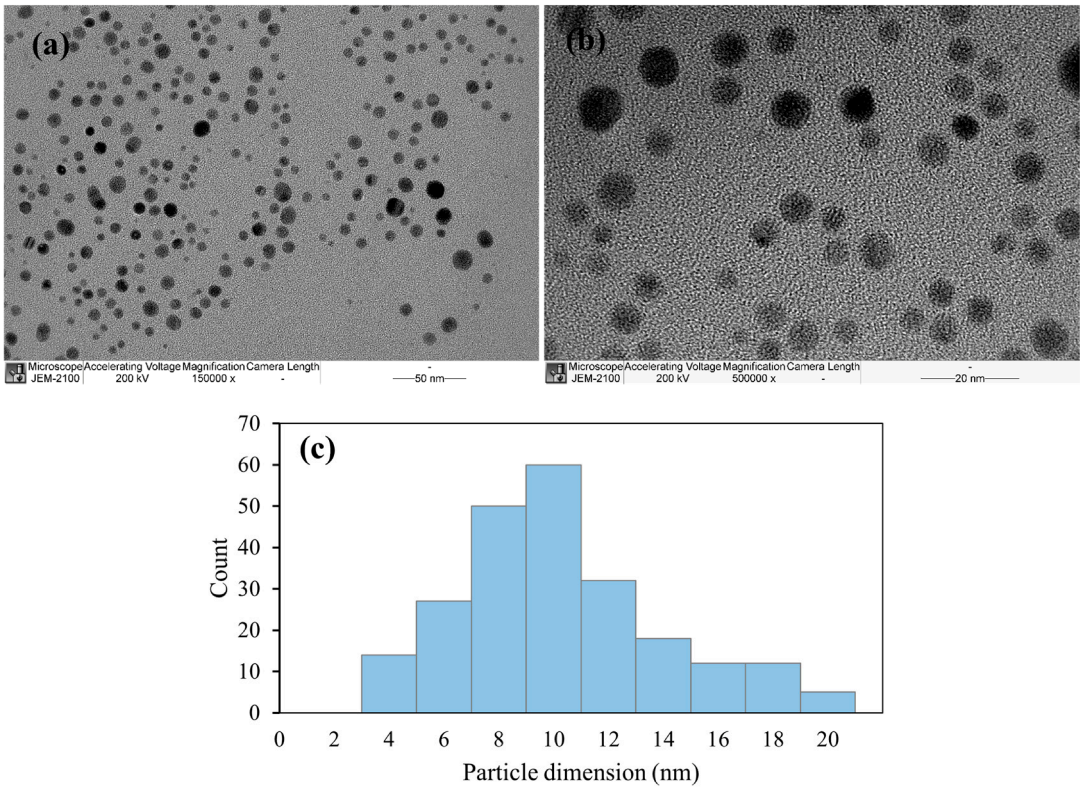


Figure 6. (**a**,**b**) TEM micrographs of biosynthesized AgNPs recorded at 250,000 × and 500,000 × magnifications, respectively, and (**c**) particle size distribution.

The colloidal stability of the ESF-AgNPs was evaluated over four weeks by monitoring zeta potential, hydrodynamic particle size, and polydispersity index (PDI), as summarized in Table 2. After 24 h, the nanoparticles exhibited a zeta potential of −35.2 ± 1.3 mV, an average hydrodynamic size of 12.1 ± 2.8 nm, and a PDI of 0.23 ± 0.02. The slightly larger size measured by dynamic light scattering than by TEM can be attributed to the hydrodynamic layer surrounding the nanoparticles, including adsorbed ESF molecules and associated water, whereas TEM measures the dried metallic particle core. During storage, the zeta potential gradually became less negative, reaching −30.1 ± 1.8 mV after four weeks. This change was accompanied by an increase in hydrodynamic size from 12.1 ± 2.8 to 15.2 ± 3.0 nm and in PDI from 0.23 ± 0.02 to 0.30 ± 0.08. These trends suggest limited particle association or gradual rearrangement of surface-bound ESF molecules. Nevertheless, the slightly increase in particle size and the absence of a pronounced increase in PDI indicate that extensive aggregation did not occur. Zeta potential values approaching zero are associated with weaker electrostatic repulsion and a greater tendency toward agglomeration, whereas absolute values of approximately 30 mV or greater generally indicate good colloidal stability [26,41]. In this study, the zeta potential remained approximately −30 mV or lower throughout the four-week period, while the PDI remained ≤0.30, indicating that the ESF-AgNP suspension retained good colloidal stability for at least one month. This result agrees with Chitichotpanya et al. [42], who reported the stabilizing role of sericin in AgNP synthesis. Similarly, ESF likely acts as both a reducing and capping agent, with its negatively charged functional groups providing electrostatic repulsion and steric stabilization that limit nanoparticle aggregation.

Table 2. Zeta potential, hydrodynamic particle size, and polydispersity index of biosynthesized ESF-AgNPs over a four-week period.

Duration	Average Zeta Potential (mV)	Average Size (nm)	PDI
24 h	−35.2 ± 1.3	12.1 ± 2.8	0.23 ± 0.02
1 week	−33.4 ± 1.2	13.4 ± 3.4	0.25 ± 0.03
2 weeks	−31.6 ± 1.4	13.8 ± 3.8	0.26 ± 0.03
4 weeks	−30.1 ± 1.8	15.2 ± 3.0	0.30 ± 0.08

3.3. Assessment of Antibacterial Activity of ESF-AgNPs

The antibacterial activity of the biosynthesized ESF-AgNPs against *V. parahaemolyticus* was evaluated using the broth microdilution and viable-count methods. As shown in Figure 7, visible bacterial growth was observed at ESF-AgNP concentrations of 0.78–6.25 µg/mL, whereas no visible turbidity was detected at concentrations of 12.5 µg/mL or higher. Therefore, the MIC was determined to be 12.5 µg/mL. The clear appearance of the wells at and above the MIC indicates the inhibition of detectable bacterial proliferation; however, it does not necessarily indicate complete bacterial killing. This distinction was confirmed by the viable-count results shown in Table 3 and Figure 8. At the MIC of 12.5 µg/mL, the viable bacterial count decreased from the initial inoculum of approximately 1.0×10^6 CFU/mL to 2.34×10^4 CFU/mL. Thus, although no visible growth was detected in the broth, viable cells could still be recovered by agar plating, indicating that this concentration primarily inhibited bacterial multiplication. At 25 µg/mL, the viable count decreased further to 4.82×10^2 CFU/mL, corresponding to a reduction of more than 3 log units and greater than 99.9% bacterial killing. Consequently, 25 µg/mL was identified as the MBC. The MBC-to-MIC ratio of 2 further indicates that the ESF-AgNPs exhibited bactericidal rather than merely bacteriostatic activity against *V. parahaemolyticus*.

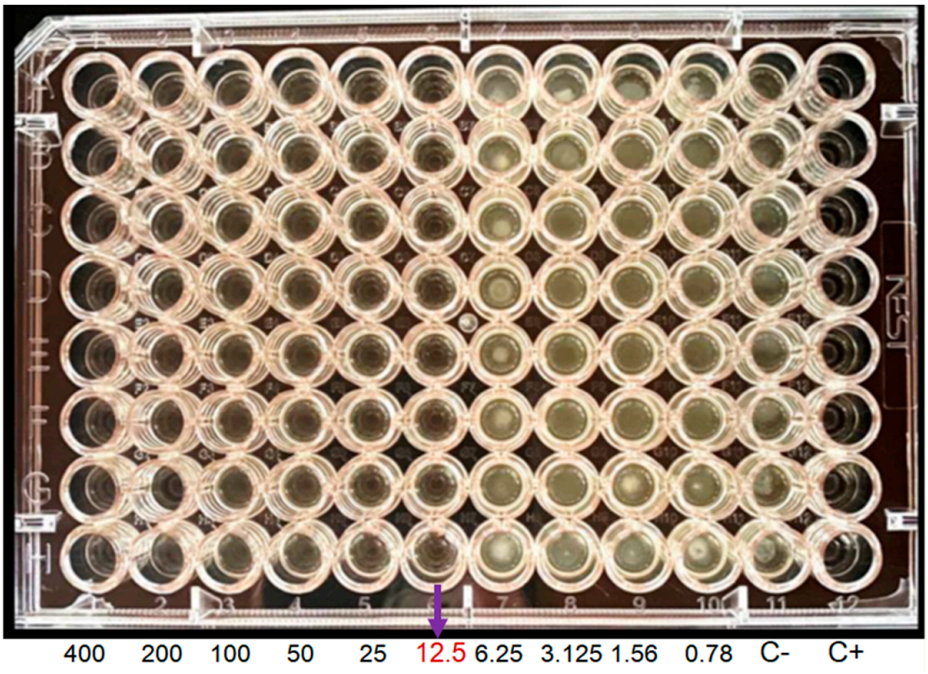


Figure 7. MIC determination of ESF-AgNPs using two-fold serial dilutions (400–0.78 µg/mL): + = Presence of bacterial growth; − = Absence of bacterial growth. The arrow indicates the MIC value (12.5 µg/mL).

Table 3. Antibacterial activity of ESF-AgNPs against *V. parahaemolyticus*.

ESF-AgNPs (µg/mL)	Visible Growth in Broth	Viable Count (CFU/mL)	Log Reduction Relative to Initial Inoculum	Reduction (%)	Interpretation
Initial inoculum	−	1.0×10^6	−	−	Baseline
0	+	8.16×10^8	−	−	Negative control
0.78	+	ND	ND	ND	Below MIC
1.56	+	ND	ND	ND	Below MIC
3.125	+	ND	ND	ND	Below MIC
6.25	+	ND	ND	ND	Below MIC
12.5	−	2.34×10^4	1.60	97.66	MIC
25	−	4.82×10^2	3.30	99.95	MBC
50	−	8.22×10^1	4.10	99.992	Bactericidal
100	−	<10	>5.00	>99.999	Below detection limit
200	−	<10	>5.00	>99.999	Below detection limit
Chloramphenicol	−	<10	>5.00	>99.999	Positive control

Values are presented as mean ± SD from three independent MBC experiments. MIC determination was conducted in five replicate wells: + = visible bacterial growth; − = no visible bacterial growth; ND = not determined.

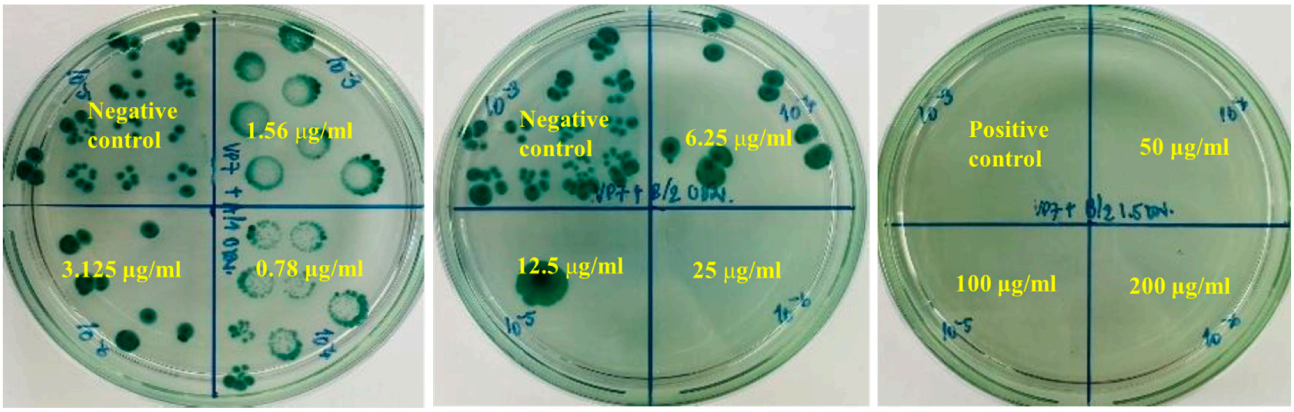


Figure 8. MBC determination of ESF-AgNPs against *V. parahaemolyticus*.

A clear concentration-dependent reduction in bacterial viability was observed. Abundant colonies were present in the untreated control and samples exposed to concentrations below the MIC, consistent with the visible growth observed in the microdilution plate. In contrast, colony recovery markedly decreased at concentrations of 12.5 µg/mL and higher. Increasing the ESF-AgNP concentration to 50 µg/mL reduced the viable count to 8.22×10^1 CFU/mL, representing an approximately 4-log reduction. At 100 and 200 µg/mL, the viable counts were below the detection limit of 10 CFU/mL, comparable to the chloramphenicol-treated positive control. These findings demonstrate progressively enhanced bacterial killing with increasing ESF-AgNP concentration. The antibacterial action of AgNPs against Vibrio species is commonly associated with their interaction with the bacterial cell envelope and the release of Ag^+ ions. Silver species can bind to membrane proteins and sulfur-containing cellular components, disrupt membrane permeability, interfere with essential enzymes, and ultimately lead to loss of cellular function and bacterial death [43]. The strong antibacterial activity observed in this study may also be related to the small size and high colloidal stability of the ESF-AgNPs. Their well-dispersed state and limited aggregation maintain a high effective surface area, facilitating contact with bacterial cells and potentially improving the availability of surface-released silver ions.

ESF-derived amino acid residues and functional groups may contribute to this performance by acting as capping and stabilizing components during nanoparticle formation. The electrostatic and steric stabilization provided by the ESF matrix limits particle aggregation and preserves nanoparticle dispersion. Previous studies have similarly suggested that the β-sheet-rich silk fibroin matrix can provide a stabilizing framework for AgNPs [19,23]. The MIC and MBC values obtained in this study were lower than those reported for biogenic AgNPs synthesized using *Camellia sinensis* [43] and *Spirulina platensis* [44] against *V. parahaemolyticus*, but slightly higher than those reported for AgNPs synthesized using *Lysinibacillus xylanilyticus* [45]. Such differences may arise from variations in nanoparticle size, surface chemistry, capping biomolecules, bacterial strains, inoculum concentrations, and experimental conditions. Therefore, the low MIC and MBC values, together with the concentration-dependent reduction in viable cells, demonstrate the strong inhibitory and bactericidal activity of ESF-AgNPs against *V. parahaemolyticus*. Beyond biogenic AgNPs, Ag-based hybrid materials have been developed to enhance antibacterial activity through complementary mechanisms and potentially reduce silver usage. Ag–TiO_2/ZIF-8, Ag–ZnO, and Ag–CuO systems have shown improved activity through combined metal-ion release, ROS generation, and membrane disruption [46,47]. Nguyen et al. [48] also reported that OEO–Ag–ZIF-8–HA exhibited MIC and MBC values of 125 and 375 μg/mL, respectively, against Listeria monocytogenes, with enhanced activity attributed to the combined effects of Ag^+, Zn^{2+}, and oregano-derived phenolic compounds. In comparison, ESF-AgNPs showed MIC and MBC values of 12.5 and 25 μg/mL, respectively, against *V. parahaemolyticus*, indicating strong antibacterial activity without the incorporation of additional inorganic or organic antibacterial components."

3.4. Antibiofilm Activity of ESF-AgNPs Against V. parahaemolyticus

ESF-AgNPs inhibited biofilm formation by *V. parahaemolyticus* in a concentration-dependent manner. Biofilm inhibition increased from 52.45 ± 3.75% at 0.25 MIC to 78.22 ± 2.41%, 91.68 ± 1.94%, and 99.98 ± 0.51% at 0.5 MIC, 1 MIC, and 2 MIC, respectively, as shown in Figure 9. Based on an MIC of 12.5 μg/mL, these concentrations corresponded to 3.125, 6.25, 12.5, and 25 μg/mL, respectively. Substantial inhibition at 0.25 MIC and 0.5 MIC is particularly notable because these concentrations were below that required to completely inhibit planktonic growth. This finding suggests that ESF-AgNPs may interfere with early biofilm-development processes, such as bacterial attachment, cell aggregation, or extracellular-matrix accumulation. Similar concentration-dependent inhibition has been reported for biopolymer-stabilized AgNPs against *V. parahaemolyticus* [28]. At 1 MIC, ESF-AgNPs reduced biofilm biomass by more than 90%, whereas treatment at 2 MIC resulted in nearly complete inhibition. At these concentrations, however, the decrease in crystal-violet staining likely reflects the combined effects of impaired biofilm development and reduced bacterial growth or viability. Therefore, the inhibition measured at MIC and 2 MIC should not be interpreted exclusively as a biofilm-specific response. The antibiofilm effect may be associated with the small size and stable dispersion of ESF-AgNPs, which facilitate interactions with bacterial cells and interfere with surface colonization and biofilm maturation. Therefore, the strong activity at both sub-MIC and inhibitory concentrations demonstrates that ESF-AgNPs effectively suppress *V. parahaemolyticus* biofilm formation. In particular, the marked inhibition at sub-MICs supports an antibiofilm effect that is not solely attributable to the complete inhibition of planktonic growth.

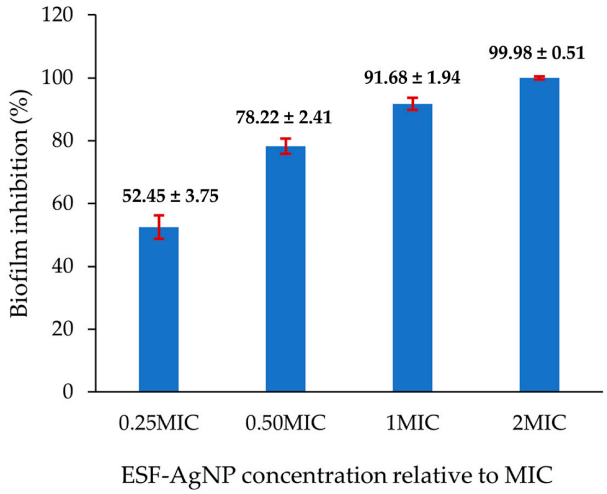


Figure 9. % Biofilm inhibition of ESF-AgNPs against *V. parahaemolyticus*.

3.5. Reactive Oxygen Species (ROS) Generation

Intracellular ROS generation in V. parahaemolyticus increased in a concentration-dependent manner following exposure to ESF-AgNPs. The untreated control was normalized to 100 ± 3%. Treatment with ESF-AgNPs at 6.25, 12.5, and 25 µg/mL, corresponding to 0.5 MIC, 1 MIC, and 1 MBC, respectively, increased the relative ROS levels to 141 ± 4%, 198 ± 7%, and 264 ± 8%, respectively (Figure 10). These values corresponded to approximately 1.41-, 1.98-, and 2.64-fold increases relative to the control, indicating that ESF-AgNPs progressively induced intracellular oxidative stress as their concentration increased. Notably, ROS production increased by 41% even at the sub-MIC of 6.25 µg/mL, suggesting that oxidative stress occurred before the complete inhibition of bacterial growth. At the MIC of 12.5 µg/mL, the ROS level was approximately twice that of the control, while exposure at the MBC of 25 µg/mL produced the highest ROS level. The enhanced ROS generation at the MIC and MBC suggests that oxidative stress may contribute to the antibacterial and bactericidal effects of ESF-AgNPs. Excessive ROS can disrupt cellular redox homeostasis and damage bacterial membranes, proteins, and nucleic acids, ultimately impairing essential cellular functions and promoting cell death [43]. Therefore, these findings support ROS generation as one of the possible antibacterial mechanisms of ESF-AgNPs against *V. parahaemolyticus*. However, because the DCFH-DA assay provides a general measure of intracellular oxidative activity, additional analyses of membrane integrity, cellular leakage, or specific ROS would be required to confirm the precise mechanism.

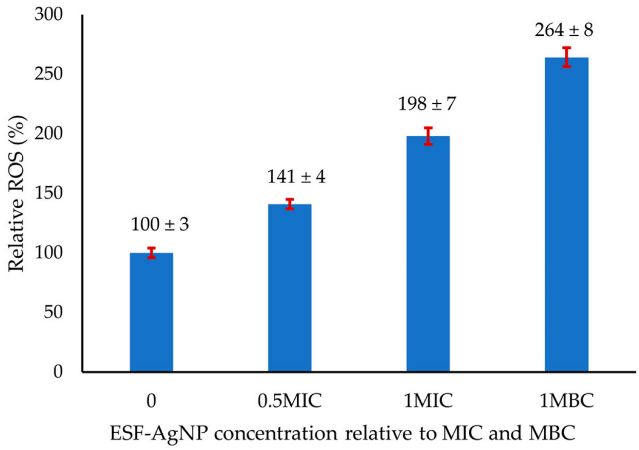


Figure 10. Intracellular reactive oxygen species (ROS) generation.

3.6. Silver Release Behavior of ESF-AgNPs

As shown in Figure 11, silver release from ESF-AgNPs increased progressively with incubation time in both DI water and TSB containing 3% NaCl. At 0 h, only 0.20 ± 0.02% and 0.40 ± 0.04% silver release was detected in DI water and TSB, respectively, which may represent weakly bound or readily desorbed silver species remaining on the nanoparticle surfaces after purification. Release increased relatively rapidly during the first 24 h, reaching 4.00 ± 0.20% in DI water and 6.50 ± 0.35% in TSB, followed by a slower increase to 5.70 ± 0.28% and 9.30 ± 0.50%, respectively, at 72 h. This profile suggests an initial release of surface-associated silver followed by slower oxidative dissolution or diffusion from the ESF-stabilized nanoparticles [49]. Silver release was consistently higher in TSB containing 3% NaCl than in DI water. The complex ionic and organic composition of the culture medium may alter nanoparticle surface interactions, colloidal behavior, and silver dissolution [50]. Our results are consistent with previous studies [51,52] which suggested that chloride ions can react with released silver to form soluble silver–chloride complexes. Because ICP-MS quantifies total silver without distinguishing among its chemical forms, the detected fraction was described as released or dissolved silver rather than exclusively as free Ag^+. Based on the initial concentration of 25 µg Ag/mL, the released silver concentrations after 72 h were approximately 1.43 µg/mL in DI water and 2.33 µg/mL in TSB containing 3% NaCl. Thus, most of the silver remained associated with the nanoparticle fraction throughout the experiment. The limited but sustained release suggests that the ESF capping restricted rapid silver dissolution while permitting gradual release under biologically relevant conditions. This interpretation is consistent with previous findings showing that surface capping biomolecules can substantially modify or reduce AgNP dissolution rates [53]. In summary, ESF-AgNPs exhibited a time-dependent and medium-dependent silver-release profile, demonstrating that silver release measurements in DI water alone may underestimate silver transformation under antibacterial assay conditions.

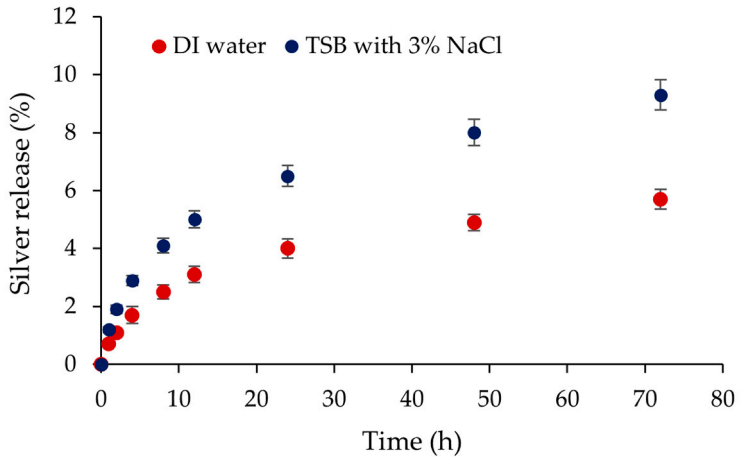


Figure 11. Time-dependent silver release from ESF-AgNPs in DI water and TSB with 3% NaCl.

3.7. Acute Toxicity of ESF-AgNPs Toward A. franciscana Nauplii

The acute toxicity assay demonstrated that ESF-AgNPs affected the survival of *A. franciscana* nauplii in a concentration- and exposure-time-dependent manner (Table 4, Figure 12). The untreated control maintained 100% survival throughout the 24 h exposure, confirming that the experimental conditions were suitable for nauplius viability. The ESF-only treatment also showed high survival of 98.5 ± 2.1% after 24 h, indicating that the ESF matrix itself caused negligible acute toxicity. At concentrations corresponding to the antibacterial range, ESF-AgNPs had only minor effects on nauplius survival. The 24 h survival rates at 6.25 and 12.5 µg/mL, equivalent to 0.5 MIC and 1 MIC, were 98.2 ± 1.1%

and 98.1 ± 1.4%, respectively. At 25 μg/mL, corresponding to 1 MBC, survival remained high at 96.2 ± 1.3%. Even at 50 μg/mL, or 2 MBC, survival was 91.9 ± 2.2%. These results suggest that the concentrations required to inhibit or kill *V. parahaemolyticus* caused limited acute toxicity toward *A. franciscana* nauplii. A more pronounced toxic effect was observed at 100 μg/mL, corresponding to 4 MBC. Survival decreased from 93.6 ± 1.9% at 6 h to 86.4 ± 1.2% at 12 h and 74.5 ± 1.0% at 24 h. This time-dependent decline may reflect cumulative nanoparticle exposure, the gradual release of Ag^+ ions, nanoparticle uptake, or interactions of silver species with the nauplius cuticle. The relatively low toxicity at the MIC and MBC values may be partly associated with stabilization of the nanoparticles by the ESF capping, which could reduce immediate silver bioavailability. In conclusion, ESF-AgNPs exhibited low acute toxicity at their MIC and MBC values, suggesting a preliminary safety margin between their antibacterial activity and acute toxicity toward *A. franciscana*.

Table 4. Survival of *A. franciscana* nauplii following acute exposure to different concentrations of ESF-AgNPs for 6, 12, and 24 h.

ESF-AgNPs (μg/mL)	Relative Concentration	Survival at 6 h (%)	Survival at 12 h (%)	Survival at 24 h (%)
0	control	100 ± 0	100 ± 0	100 ± 0
ESF only	Matrix control	100 ± 0	100 ± 0	98.5 ± 2.1
6.25	0.5 MIC	100 ± 0	99.1 ± 0.6	98.2 ± 1.1
12.5	1 MIC	99.0 ± 2.6	98.7 ± 1.4	98.1 ± 1.4
25	1 MBC	97.3 ± 2.5	96.0 ± 2.2	96.2 ± 1.3
50	2 MBC	97.2 ± 2.8	94.0 ± 2.1	91.9 ± 2.2
100	4 MBC	93.6 ± 1.9	86.4 ± 1.2	74.5 ± 1.0

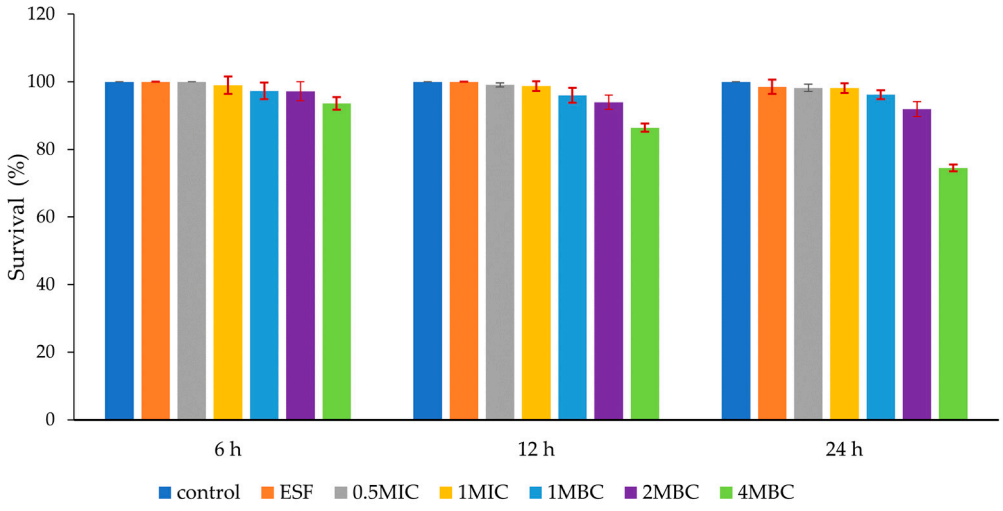


Figure 12. Survival of *A. franciscana* nauplii following exposure to ESF-AgNPs at different concentrations for 6, 12, and 24 h.

3.8. Study Limitations and Future Perspectives

Several limitations should be acknowledged. First, the cytotoxicity of ESF-AgNPs toward shrimp-derived cells, tissues, or whole organisms was not evaluated. Although the acute toxicity assay using *A. franciscana* provided preliminary short-term biosafety information, Artemia is not a direct surrogate for shrimp. Therefore, further studies using shrimp-derived cells and in vivo exposure models are required to establish appropriate safety margins and tissue-specific effects. Second, the silver-release and acute-toxicity

tests do not constitute a comprehensive environmental risk assessment. Further studies on chronic toxicity, environmental transformation, persistence, bioaccumulation, trophic transfer, and effects on non-target aquatic organisms are required before practical application. Finally, antibacterial activity was evaluated using a single AHPND-associated Vibrio parahaemolyticus isolate. Because the *pirA* and *pirB* toxin genes were not confirmed, the isolate cannot be conclusively classified as a toxigenic AHPND-causing strain. Future studies should confirm its genotype, test multiple well-characterized isolates, and conduct in vivo shrimp challenge experiments.

4. Conclusions

ESF successfully served as both a reducing and stabilizing biopolymer for AgNP biosynthesis. The optimal conditions, comprising an $AgNO_3$-to-ESF weight ratio of 1:4, a reaction temperature of 60 °C, and a reaction time of 4 h, produced a high yield of small, uniformly distributed nanoparticles with a strongly negative zeta potential and low PDI. FTIR analysis indicated the involvement of hydroxyl-, amide-, and tyrosine-associated groups in Ag^+ reduction and nanoparticle stabilization. TEM, XRD, and XPS confirmed the formation of predominantly spherical, crystalline Ag^0 nanoparticles. The ESF-AgNPs remained colloidally stable for at least four weeks. The ESF-AgNPs showed potent concentration-dependent activity against *V. parahaemolyticus*, with MIC and MBC values of 12.5 and 25 μg/mL, respectively. They also strongly suppressed biofilm formation, including substantial inhibition at sub-MICs, and induced concentration-dependent intracellular ROS generation, supporting oxidative stress as a possible antibacterial mechanism. Silver release occurred gradually and was greater in TSB containing 3% NaCl than in DI water, demonstrating that the composition of the antibacterial-test medium influenced silver transformation and availability. Importantly, ESF alone exhibited negligible acute toxicity toward *A. franciscana*, and nauplius survival remained high at the MIC and MBC, indicating a preliminary safety margin between antibacterial efficacy and acute aquatic toxicity. These findings demonstrate that ESF provides a sustainable platform for producing AgNPs with potent antibacterial and antibiofilm activities against *V. parahaemolyticus*, while exhibiting a preliminary safety margin at effective antibacterial concentrations. Nevertheless, further studies on in vivo efficacy, chronic toxicity, and environmental-fate are required before their practical application in aquaculture can be established.

Author Contributions: Conceptualization, P.C. and C.C.; methodology, N.V., P.P. and M.J.; validation, N.V., M.J. and C.C.; formal analysis, P.C.; investigation, M.J., P.P. and N.V.; resources, P.C. and C.C.; data curation, M.J. and P.P.; writing—original draft preparation, P.C. and C.C.; writing—review and editing, C.C. and P.C.; visualization, N.V. and P.C.; supervision, C.C. and P.C. All authors have read and agreed to the published version of the manuscript.

Funding: This research was supported by the Thailand Science Research and Innovation (TSRI) Fundamental Fund, fiscal year 2026.

Data Availability Statement: The raw data supporting the conclusions of this article will be made available by the authors on request.

Acknowledgments: This research was financially supported by the Thailand Science Research and Innovation (TSRI) Fundamental Fund, fiscal year 2026. Additional support was provided by the Thammasat University Center of Excellence in Smart Materials, Energy, Biochemistry, Food Technology, and Textile Innovation for a Sustainable Environment. During the preparation of this manuscript, ChatGPT 5.2 (OpenAI) was used to improve the clarity, grammar, and overall coherence of the English language. The authors reviewed and edited all AI-generated content and take full responsibility for the accuracy and integrity of the final manuscript.

Conflicts of Interest: The authors declare no conflicts of interest.

References

1. Campbell, E.; Becker, J.A.; Bracher, P.; Budhiraja, B.; Chaiyapechara, S.; Chen, W.N.; Colyer, L.; Karoonuthaisiri, N.; Keeffe, G.; McKinley, J.; et al. Challenges and strategies for globally resilient shrimp aquaculture. *npj Sci. Food* **2026**, *10*, 140. [CrossRef] [PubMed]
2. Kittichotsatsawat, Y.; Wattanutchariya, W.; Jongjareonrak, A.; Seesuriyachan, P. Enhancing manufacturing operations within the supply chain for sustainable frozen shrimp production. *Sustainability* **2025**, *17*, 2412. [CrossRef]
3. Santos, H.M.; Tsai, C.; Maquiling, K.R.A.; Tayo, L.L.; Mariatulqabtiah, A.R.; Lee, C.; Chuang, K.P. Diagnosis and potential treatments for acute hepatopancreatic necrosis disease (AHPND): A review. *Aquac. Int.* **2020**, *28*, 169–185. [CrossRef] [PubMed]
4. Zheng, X.; Guo, J.; Rao, H.; Guo, D.; Huang, Y.; Xu, Y.; Liang, S.; Xia, X.; Shi, C. Antibacterial and antibiofilm activity of coenzyme Q0 against *Vibrio parahaemolyticus*. *Food Control* **2020**, *109*, 106955. [CrossRef]
5. Kumar, V.; Roy, S.; Behera, B.K.; Bossier, P.; Das, B.K. Acute Hepatopancreatic Necrosis Disease (AHPND): Virulence, pathogenesis and mitigation strategies in shrimp aquaculture. *Toxins* **2021**, *13*, 524. [CrossRef] [PubMed]
6. Preeprem, S.; Aksonkird, T.; Nuidate, T.; Hajimasalaeh, W.; Hajiwangoh, Z.; Mittraparp-arthorn, P. Characterization and genetic relationships of Vibrio spp. isolated from seafood in retail markets, Yala, Thailand. *Trends Sci.* **2023**, *20*, 5962. [CrossRef]
7. Xin, Y.; Shurui, P.; Wei, S.; Lei, Y.; Zhang, S.; Hu, Y.; Lv, Y. Antimicrobial and biofilm inhibition effects of p-anisaldehyde against *Vibrio parahaemolyticus*. *Food Control* **2023**, *154*, 110021.
8. Elmahdi, S.; LV Dasilva, L.V.; Parveen, S. Antibiotic resistance of *Vibrio parahaemolyticus* and *Vibrio vulnificus* in various countries: A review. *Food Microbiol.* **2016**, *7*, 128–134.
9. Tan, C.W.; Rukayadi, Y.; Hasan, H.; Thung, T.Y.; Lee, E.; Rollon, W.D.; Hara, H.; Kayali, A.Y.; Nishibuchi, M.; Radu, S. Prevalence and antibiotic resistance patterns of *Vibrio parahaemolyticus* isolated from different types of seafood in Selangor, Malaysia. *Saudi J. Biol. Sci.* **2020**, *27*, 1602–1608. [CrossRef] [PubMed]
10. Tan, X.; Qiao, J.; Wang, J.; Li, H.; Wang, X. Characterization of ampicillin-resistant genes in *Vibrio parahaemolyticus*. *Microb. Pathog.* **2022**, *168*, 105573. [PubMed]
11. Bentzon-Tilia, M.; Sonnenschein, E.C.; Gram, L. Monitoring and managing microbes in aquaculture—Towards a sustainable industry. *Microb. Biotechnol.* **2016**, *9*, 576–584. [CrossRef] [PubMed]
12. Prabhu, C.; Satyaprasad, A.U.; Deekshit, V.K. Understanding bacterial resistance to heavy metals and nanoparticles: Mechanisms, implications, and challenges. *J. Basic Microbiol.* **2025**, *65*, e2400596. [PubMed]
13. Bhatt, K.; Anita, K.; Atharb, M.; Jain, V. New views on the ingenious applications of Ag nanoparticles as a sensor for antibiotic detection and as a potent antimicrobial agent. *J. Met. Mater. Miner.* **2021**, *31*, 1–9.
14. Camacho-Jiménez, L.; Álvarez-Sánchez, A.R.; Mejía-Ruíz, C.H. Silver nanoparticles (AgNPs) as antimicrobials in marine shrimp farming: A review. *Aquac. Rep.* **2020**, *18*, 100512.
15. Magdy, G.; Aboelkassim, E.; Elhaleem, S.M.; Belal, F. A comprehensive review on silver nanoparticles: Synthesis approaches, characterization techniques, and recent pharmaceutical, environmental, and antimicrobial applications. *Microchem. J.* **2024**, *196*, 109615. [CrossRef]
16. Zhou, B.; Wang, H. Structure and Functions of Cocoons Constructed by Eri Silkworm. *Polymers* **2020**, *12*, 2701. [CrossRef] [PubMed]
17. Chartvivatpornchai, N.; Okahisa, Y. Structural and mechanical comparison of Eri and Mulberry silk fibroin nanofibers films through advanced mechanical treatments for sustainable applications. *Int. J. Biol. Macromol.* **2025**, *295*, 139554. [PubMed]
18. Shivananda, C.S.; Lakshmeesha Rao, B.; Sangappa. Structural, thermal and electrical properties of silk fibroin–silver nanoparticles composite films. *J. Mater. Sci. Mater. Electron.* **2020**, *31*, 41–51. [CrossRef]
19. Shivananda, C.S. Silk fibroin-based green colloidal silver nanoparticle synthesis and their antibacterial and anticancer properties. *Inorg. Chem. Commun.* **2023**, *158*, 111611. [CrossRef]
20. Sangappa, Y.; Latha, S.; Asha, S.; Sindhu, P.; Parushuram, N.; Shilpa, M.; Byrappa, K.; Narayana, B. Synthesis of anisotropic silver nanoparticles using silk fibroin: Characterization and antimicrobial properties. *Mater. Res. Innov.* **2019**, *23*, 79–85.
21. Alavi, M.; Varma, R.S. Antibacterial and wound healing activities of silver nanoparticles embedded in cellulose compared to other polysaccharides and protein polymers. *Cellulose* **2021**, *28*, 8295–8311. [CrossRef]
22. Simon, S.; Sibuyi, N.R.S.; Fadaka, A.O.; Meyer, S.; Josephs, J.; Onani, M.O.; Meyer, M.; Madiehe, A.M. Biomedical Applications of Plant Extract-Synthesized Silver Nanoparticles. *Biomedicines* **2022**, *10*, 2792. [CrossRef] [PubMed]
23. Brahma, B.B.; Wary, R.R.; Narzary, M.; Kalita, P.; Basumatary, Z.; Baruah, M.B. Eri silk fibroin derived silver nanoparticles for antibacterial and photocatalytic applications. *Inorg. Chem. Commun.* **2025**, *171*, 113593. [CrossRef]
24. Xue, Y.; Wang, F.; Torculas, M.; Lofland, S.; Hu, X. Formic acid regenerated Mori, Tussah, Eri, Thai, and Muga silk materials: Mechanism of self-assembly. *ACS Biomater. Sci. Eng.* **2019**, *5*, 6361–6373. [CrossRef] [PubMed]
25. Agnihotri, S.; Mukherji, S.; Mukherji, S. Size-controlled silver nanoparticles synthesized over the range 5–100 nm using the same protocol and their antibacterial efficacy. *RSC Adv.* **2014**, *4*, 3974–3983. [CrossRef]

26. Jariyaboon, M.; Masrinoul, P.; Komaikul, J.; Muenkaew, K.; Juntarapornchai, S.; Ketsuwan, K.; Rodpai, E.; Ruangdachsuwan, S.; Palabodeewat, S.; Chitichotpanya, C. Optimization of Ag-TiO2 nanocomposite at a low toxicity dose as a self-virucidal disinfectant against COVID-19. *Emergent Mater.* **2023**, *6*, 1259–1272. [CrossRef]
27. CLSI. *Performance Standards for Antimicrobial Susceptibility Testing: 24th Informational Supplement, CLSI Document M100-S24*; Clinical and Laboratory Standards Institute: Wayne, PA, USA, 2014.
28. Yuan, C.; Zhan, W.; Cui, Q. Antibacterial activity and mechanism of the gallnut water extract against *Vibrio parahaemolyticus*. *J. Aquat. Anim. Health* **2022**, *34*, 159–166. [CrossRef] [PubMed]
29. Zamanpour, N.; Esmaeily, A.M.; Mashreghi, M.; Shahnavaz, B.; Sharifmoghadam, M.R.; Kompany, A. Application of a marine luminescent Vibrio sp. B4L for biosynthesis of silver nanoparticles with unique characteristics, biochemical properties, antibacterial and antibiofilm activities. *Bioorg. Chem.* **2021**, *114*, 105102. [CrossRef] [PubMed]
30. Nongsok, S.; Vanichvattanadecha, C.; Pisitsak, P. Lignin- and Silver-Modified Multifunctional Cotton Fabrics: Influence of α- and β-Chitosan Pretreatment on Structure–Property Relationships. *Polymers* **2026**, *18*, 1279. [CrossRef] [PubMed]
31. Latha, M.; Priyanka, M.; Rajasekar, P.; Manikandan, R.; Prabhu, N.M. Biocompatibility and antibacterial activity of the Adathoda vasica Linn. extract-mediated silver nanoparticles. *Microb. Pathog.* **2016**, *93*, 88–94. [CrossRef] [PubMed]
32. Alvarez-Cirerol, F.J.; López-Torres, M.A.; Rodríguez-León, E.; Rodríguez-Beas, C.; Martínez-Higuera, A.; Lara, H.H.; Vergara, S.; Arellano-Jiménez, M.J.; Larios-Rodríguez, E.; Martínez-Porchas, M.; et al. Silver nanoparticles synthesized with Rumex hymenosepalus: A strategy to combat early mortality syndrome (EMS) in a cultivated white shrimp. *J. Nanomater.* **2019**, *2019*, 8214675. [CrossRef]
33. Alzoubi, F.Y.; Ahmad, A.A.; Aljarrah, I.A.; Migdadi, A.B.; Al-Bataineh, Q.M. Localize surface plasmon resonance of silver nanoparticles using Mie theory. *J. Mater. Sci. Mater. Electron.* **2023**, *34*, 2128. [CrossRef]
34. Liu, H.; Zhang, H.; Wang, J.; Wei, J. Effect of temperature on the size of biosynthesized silver nanoparticle: Deep insight into microscopic kinetics analysis. *Arab. J. Chem.* **2017**, *13*, 1011–1019.
35. Gwada, C.A.; Ndivhuwo, P.S.; Matshetshe, K.; Aradi, E.; Mdluli, P.; Moloto, N.; Otieno, F.; Airo, M. Phytochemical-assisted synthesis, optimization, and characterization of silver nanoparticles for antimicrobial activity. *RSC Adv.* **2025**, *15*, 14170–14181. [CrossRef] [PubMed]
36. Chen, M.; Feng, Y.; Wang, X.; Li, T.; Zhang, J.; Qian, D. Silver nanoparticles capped by oleyl amine: Formation, growth, and self-organization. *Langmuir* **2007**, *23*, 5296–5304. [CrossRef] [PubMed]
37. Ke, J.; Zhu, Y.; Zhang, J.; Yang, J.; Guo, H.; Zhao, W.; Wen, C.; Zhang, L. Size-dependent uptake and distribution of AgNPs by silkworms. *ACS Sustain. Chem. Eng.* **2019**, *8*, 460–468. [CrossRef]
38. Chitichotpanya, C.; Khwanmuang, P.; Yamprayoonswat, W.; Porntheeraphat, S.; Jongkaewwattana, A.; Chitichotpanya, P. Potent environmental-friendly virucidal medical textiles against coronavirus to combat infections during the COVID-19 pandemic. *J. Ind. Text.* **2022**, *51*, 6996S–7013S. [CrossRef] [PubMed]
39. Kim, M.; Jee, S.-C.; Shinde, S.K.; Mistry, B.M.; Saratale, R.G.; Saratale, G.D.; Ghodake, G.S.; Kim, D.-Y.; Sung, J.-S.; Kadam, A.A. Green-synthesis of anisotropic peptone-silver nanoparticles and its potential application as anti-bacterial agent. *Polymers* **2019**, *11*, 271. [CrossRef] [PubMed]
40. Abdelgawad, A.M.; El-Naggar, M.E.; Eisa, W.H.; Rojas, O.J. Clean and high-throughput production of silver nanoparticles mediated by soy protein via solid state synthesis. *J. Clean. Prod.* **2017**, *144*, 501–510. [CrossRef]
41. RathnaKumari, P.; Kolanchinathan, P.; Siva, D.; Abirami, B.; Masilamani, V.; John, G.; Achiraman, S.; Balasundaram, A. Antibacterial efficacy of seagrass *Cymodocea serrulata*-engineered silver nanoparticles against prawn pathogen *Vibrio parahaemolyticus* and its combative effect on the marine shrimp Penaeus monodon. *Aquaculture* **2018**, *493*, 158–164. [CrossRef]
42. Chitichotpanya, P.; Chitichotpanya, C. In Vitro Assessment of Sericin-Silver Functionalized Silk Fabrics for Enhanced UV Protection and Antibacterial Properties Using Experimental Design. *Coatings* **2017**, *7*, 145. [CrossRef]
43. I, S.K.; Soundharajan, R.; Srinivasan, H. *Camellia sinensis* mediated nanoparticles to control growth and biofilm in Vibrio sp. *Aquac. Int.* **2025**, *33*, 204. [CrossRef]
44. Haque, E.; Kumarasamy, R. Bioengineered silver nanoparticle from *Spirulina platensis* in attenuating biofilm mediated virulence in *Vibrio parahemolyticus*: An in vitro and in vivo approach. *Int. J. Pharm. Investig.* **2020**, *10*, 486–491. [CrossRef]
45. Huq, M.A. Biogenic silver nanoparticles synthesized by *Lysinibacillus xylanilyticus* MAHUQ-40 to control antibiotic-resistant human pathogens *Vibrio parahaemolyticus* and *Salmonella Typhimurium*. *Front. Bioeng. Biotechnol.* **2020**, *8*, 1407. [CrossRef]
46. Rathi, V.H.; Jeice, A.R.; Jayakumar, K. Green synthesis of Ag/CuO and Ag/TiO_2 nanoparticles for enhanced photocatalytic dye degradation, antibacterial, and antifungal properties. *Appl. Surf. Sci. Adv.* **2023**, *18*, 100476. [CrossRef]
47. Nguyen, H.L.; Moreira, R.G.; Castell-Perez, M.E. Antibacterial effectiveness of zeolitic imidazolate framework-8 (ZIF-8) nanoparticle solutions and their derivatives against Salmonella Typhimurium ATCC 13311 on loose-leaf lettuce. *J. Food Saf.* **2025**, *45*, e70031. [CrossRef]
48. Nguyen, H.L.; Moreira, R.G.; Castell-Perez, M.E. Multifunctional OEO-ZIF-8-HA nanoparticles for antibacterial control on latex surfaces and baby arugula (Eruca sativa) leaves. *J. Food Sci.* **2026**, *91*, e70896. [CrossRef] [PubMed]

49. Liu, J.; Hurt, R.H. Ion release kinetics and particle persistence in aqueous nano-silver colloids. *Environ. Sci. Technol.* **2010**, *44*, 2169–2175. [CrossRef] [PubMed]
50. Mat Lazim, Z.; Salmiati, S.; Marpongahtun, M.; Arman, N.Z.; Mohd Haniffah, M.R.; Azman, S.; Yong, E.L.; Salim, M.R. Distribution of silver (Ag) and silver nanoparticles (AgNPs) in aquatic environment. *Water* **2023**, *15*, 1349. [CrossRef]
51. Li, Y.; Zhao, J.; Shang, E.; Xia, X.; Niu, J.; Crittenden, J. Effects of chloride ions on dissolution, ROS generation, and toxicity of silver nanoparticles under UV irradiation. *Environ. Sci. Technol.* **2017**, *52*, 4842–4849. [CrossRef] [PubMed]
52. Yonathan, K.; Mann, R.; Mahbub, K.R.; Gunawan, C. The impact of silver nanoparticles on microbial communities and antibiotic resistance determinants in the environment. *Environ. Pollut.* **2022**, *293*, 118506. [CrossRef] [PubMed]
53. Liu, C.; Leng, W.; Vikesland, P.J. Controlled evaluation of the impacts of surface coatings on silver nanoparticle dissolution rates. *Environ. Sci. Technol.* **2018**, *52*, 2726–2734. [CrossRef] [PubMed]

Disclaimer/Publisher's Note: The statements, opinions and data contained in all publications are solely those of the individual author(s) and contributor(s) and not of MDPI and/or the editor(s). MDPI and/or the editor(s) disclaim responsibility for any injury to people or property resulting from any ideas, methods, instructions or products referred to in the content.